Synthesis of a hybrid nanostructure of ZnO-decorated MoS_2 by atomic layer deposition

Oh, Il-Kwon; Kin, Woo-Hee; Zeng, Li; Singh, Joseph; Bae, Dowon; Mackus, Adriaan J.M.; Song, Jeong-Gyu; Seo, Seunggi; Song, Bonggeun

DOI
10.1021/acsnano.9b07467

Publication date
2020

Document Version
Accepted author manuscript

Published in
ACS Nano

Citation (APA)
Oh, I.-K., Kin, W.-H., Zeng, L., Singh, J., Bae, D., Mackus, A. J. M., Song, J.-G., Seo, S., & Song, B. (2020). Synthesis of a hybrid nanostructure of ZnO-decorated MoS_2 by atomic layer deposition. *ACS Nano*, *14*(2), 1757-1769. https://doi.org/10.1021/acsnano.9b07467

Oh et al., ACS Nano 2020
Cite This: https://dx.doi.org/10.1021/acsnano.9b07467

Synthesis of a Hybrid Nanostructure of ZnO-Decorated MoS_2 by Atomic Layer Deposition

Il-Kwon Oh[a,b,#], Woo-Hee Kim[a,c,#], Li Zeng[a], Joseph Singh[d], Dowon Bae[e], Adriaan J. M. Mackus[a], Jung-Gyu Song[b], Seunggi Seo[b], Bonggeun Shong[f], Hyungjun Kim[b], and Stacey F. Bent[a,c,]*

[a] *Department of Chemical Engineering, Stanford University, CA 94305, USA*

[b] *School of Electrical and Electronic Engineering, Yonsei University, Seoul 03722, Korea*

[c] *Department of Materials Science and Chemical Engineering, Hanyang University, Ansan 15588, Korea*

[d] *Department of Chemistry, Stanford University, CA 94305, USA*

[e] *Materials for Energy Conversion and Storage (MECS), Department of Chemical Engineering, Delft University of Technology, Delft 2600 AA, Netherland*

[f] *Department of Chemical Engineering, Hongik University, Seoul 04066, Korea*

*Corresponding author's email: sbent@stanford.edu

ABSTRACT

We introduce the synthesis of hybrid nanostructures comprised of ZnO nanocrystals (NCs) decorating nanosheets and nanowires (NWs) of MoS_2 prepared by atomic layer deposition (ALD). The concentration, size, and surface-to-volume ratio of the ZnO NCs can be systematically engineered by controlling both the number of ZnO ALD cycles and the properties of the MoS_2 substrates, which are prepared by sulfurizing ALD MoO_3. Analysis of the chemical composition combined with electron microscopy and synchrotron X-ray techniques as a function of the number of ZnO ALD cycles, together with the results of quantum chemical calculations, help elucidate the ZnO growth mechanism and its dependence on the properties of the MoS_2 substrate. The defect density and grain size of MoS_2 nanosheets are controlled by the sulfurization temperature of ALD MoO_3, and the ZnO NCs in turn nucleate selectively at defect sites on MoS_2 surface and enlarge with increasing ALD cycle numbers. At higher ALD cycle numbers, the coalescence of ZnO NCs contributes to an increase in areal coverage and NC size. Additionally, the geometry of the hybrid structures can be tuned by changing the dimensionality of the MoS_2, by employing vertical NWs of MoS_2 as the substrate for ALD ZnO NCs, which in turn leads to improvement of the relevant surface-to-volume ratio. Such materials are expected to find use in newly expanded applications, especially those such as sensors or photo-devices based on a *p-n* heterojunction which relies on coupling transition metal dichalcogenides (TMDCs) with NCs.

KEYWORDS: hybrid nanostructure, ZnO-decorated MoS_2 nanosheets, ZnO-decorated MoS_2 nanowires, atomic layer deposition

Recently, transition metal dichalcogenide (TMDC) 2D materials have generated intense interest due to their interesting structures and properties as well as their importance to various applications, including sensors,[1] catalysts,[2] photonics,[3] and energy storage.[4] MoS_2, which has become the most representative 2D TMDC, has attracted much attention because it has the following attributes: a direct band gap (1.8 eV), high surface-to-volume ratio relative to bulk semiconductors, and outstanding field-effect transistor (FET) behavior.[5] However, many opportunities still exist to develop new synthetic strategies to tune the properties of MoS_2 nanostructures for advanced applications.

Decorating MoS_2 with nanocrystals (NCs) has significantly expanded the applications for MoS_2. At the same time that these decorated structures maintain the individual properties of each component, they provide synergistic characteristics resulting from the combined materials. For example, Pt–MoS_2 nanohybrids exhibit much higher electrocatalytic activity toward hydrogen evolution reaction (HER)[6] and electrocatalytic methanol oxidation[7] compared to commercial Pt catalysts. Nevertheless, most studies to date have focused on decorating MoS_2 nanostructures with a small set of noble metal nanoparticles (*e.g.*, Pt, Pd, Ag, and Au).[6,8] Currently, there have been only limited reports on MoS_2 functionalized with NCs of other materials such as metal oxides; examples include MoS_2 nanostructures coated with TiO_2 nanobelts which showed high performance in photocatalytic properties;[9] the *p*-type semiconductor Cu_2O decorating MoS_2 nanostructures, which led to an increase in solar hydrogen production;[10] and, ZnO on MoS_2, which will be discussed below.

ZnO provides an interesting metal oxide system for decorating MoS_2 structures. ZnO is an attractive *n*-type semiconductor which has been widely studied for a variety of applications[11,12] due to its good response of gas sensing and photo-detection, environmental friendliness, relatively low production cost, and simple synthesis process with size-controllability.[13,14] Since MoS_2 nanosheets act as a narrow band gap, *p*-type semiconductor and ZnO serves as a wide band gap (3.37 eV), *n*-type semiconductor, a hybrid system allows the construction of a *p*-*n* heterojunction.[9,15,16] The built-in potential in this ZnO/MoS_2 *p*-*n* junction leads to separation of electron/hole pairs and resultant current flow, so better performance may be achieved in applications such as sensors and photo-devices compared to a single ZnO or MoS_2 system.

Controlling the morphology of the ZnO NCs including their concentration, size and surface-to-volume ratio is crucial for the overall performance of electronic devices.[17-19] Hence, developing a synthesis process for fabricating ZnO/MoS_2 hybrids with tunable morphology is important. There have been a few reports on the synthesis of ZnO/MoS_2 hybrids by several techniques to grow ZnO, including a hydrothermal method,[20,21] atomic layer deposition (ALD),[22-24] and a solvothermal method.[25] Kang *et al.* reported ALD of ZnO that was indirectly used to make ZnO/MoS_2 assemblies by depositing ZnO films on Si onto which MoS_2 nanostructures were then transferred.[22] On the other hand, using ALD to achieve direct decoration of NCs on 2D materials is especially promising because it allows one to take advantage of ALD's inherent growth characteristics and NC-size controllability.[26-28] In particular, because ALD is based on self-limiting chemical reactions at the surface, the lack of chemically reactive surface groups on 2D materials should permit selective decoration of the 2D material with NCs in which the NC size can be atomically controlled by cycle number.[26] For example, Walter *et al.* recently presented ALD ZnO on bulk crystal MoS_2 and showed island growth of ZnO NCs by comparing morphologies before and after ALD.[23] Kang *et al.* recently described ALD ZnO with varying ALD cycle numbers on MoS_2 that had been prepared by a hydrothermal method and applied the resulting structures to photodetectors.[24] However, because they mainly focused on fabricating uniform ZnO layers on

MoS_2 substrates, none of the previous studies examined the detailed mechanisms of ZnO nucleation and growth on MoS_2 by ALD nor on controlling the morphologies of the resulting ZnO NCs. Since the size and distribution of NCs govern the overall performance of NC-decorated MoS_2 devices, understanding how to control the morphologies of ZnO NCs requires more attention.

In this work, we introduce the ALD-assisted synthesis of hybrid nanostructures comprised of ZnO NCs decorating MoS_2, in which the morphologies of the NCs are tuned by controlling the synthesis conditions of both MoS_2 and ZnO. The MoS_2 system provides an excellent platform for controlled 0D NC deposition when the ALD technique is employed. Since the number of chemically reactive surface groups on MoS_2, which serve as the nucleation sites for ALD ZnO, depends strongly on the sulfurization temperature of MoO_3,[29] the system provides an additional lever for systematically tuning the concentration of the ZnO NCs through the MoS_2 annealing temperature, while the NC size is governed by the ZnO ALD cycles. To achieve the hybrid nanostructures, the MoS_2 quality, defined by defect density and grain size, was varied by changing the temperature at which ALD MoO_3 was sulfurized to MoS_2. ZnO was subsequently deposited on the MoS_2 structures as a function of ALD cycle number. The ZnO nucleation and growth mechanisms were studied by correlating different characterization results, including vibrational energy states, atomic scale images by electron microscopy, synchrotron X-ray scattering patterns, surface chemical compositions and morphology. The experimental results were complemented by theoretical calculations. This combined experimental and theoretical study on ZnO-decorated MoS_2 hybrid nanostructures should significantly expand the applications of such nanostructures.

RESULTS AND DISCUSSION

MoS_2 nanosheets and NWs are fabricated by the two-step sulfurization process from ALD-grown MoO_3, as described in Methods and shown schematically in Figure 1(a). Raman spectroscopy is performed on the 600 ^oC-, 800 ^oC-, and 1000 ^oC-MoS_2 nanosheet samples to examine the sulfurized film quality, with the resulting spectra shown in Figure 1(b). Note that the Raman-active vibrational modes are polarization-dependent and the intensity and positions of the modes depend on the layer stacking sequence of the MoS_2 film;[30] the polarization of the vibrational E^1_{2g} mode (symmetric) and the A_{1g} mode (anti-symmetric) are along the in-plane and out-of-plane direction, respectively.[31] The three annealed films exhibit both in-plane and out-of-plane peaks near 383.5 and 403.6 cm^{-1}, respectively, corresponding to vibrational modes of MoS_2 nanosheets.[31] In addition, the E^1_{2g} and A_{1g} peak separation of 23.2 cm^{-1} indicates that the MoS_2 nanosheets are multilayers comprised of more than three layers.[31]

The height and width of the Raman E^1_{2g} and A_{1g} modes provide information on the degree of crystallinity of the MoS_2 layers. Both Raman peaks become sharper and more intense at higher peak annealing temperatures, which indicates improved structural quality of MoS_2. The full width at half maximum (FWHM) values of the A_{1g} and E^1_{2g} peaks are presented in Figure 1(c). The FWHM decreases from 10.7 to 5.2 cm^{-1} for the A_{1g} peak and decreases from 14.9 to 6.0 cm^{-1} for the E^1_{2g} peak when the annealing temperature is raised from 600 to 1000 ℃. The broadening of the Raman peaks for MoS_2 sulfurized at lower annealing temperature can be attributed to several factors. The main factor is the crystal structure of the film, *i.e.*, whether it is polycrystalline or a mixed structure of horizontal and vertical growth.[32] Other factors are poor crystallinity due to defects existing in the crystal and finite grain size.[29] The narrower spectral line-width of films made at 1000 ℃, compared to their counterparts synthesized at lower temperatures, thus indicates the formation of the highest quality crystalline film at the highest temperature studied.

The crystalline structure of the MoS_2 substrates was probed by grazing incidence wide-angle X-ray scattering (GIWAXS), shown in Figure S1 in Supporting Information. The crystallite size of MoS_2 (002) increases about 10% as annealing temperature is increased from 600 ℃ to 1000 ℃ (from 36.7 Å to 39.0 Å). The trend of increased MoS_2 crystallinity with increased annealing temperature agrees with what we observed from Raman spectra shown in Figure 1(b) and 1(c). This increased crystallinity of MoS_2 as the annealing temperature increases corresponds to previous reports,[30,33] indicating that the density of dislocations and defects in MoS_2 decreases with increase in annealing temperature resulting in improvement of the crystalline quality.[45] Also, the crystalline structure of the 800 ℃-MoS_2 material was further observed by high-resolution scanning transmission electron microscopy (HR-STEM) shown in Figure 1(d). The image shows periodically arranged atoms with several different orientations of crystalline MoS_2 planes. 1D grain boundaries, highlighted by white dashed lines, are seen. The lateral size of the crystallites is in the range of 4 ~ 30 nm. Additionally, Moiré patterns indicate that the MoS_2 films are multilayers containing more than three layers.[34]

Figure 1(e) and 1(f) show X-ray photoelectron spectroscopy (XPS) spectra of the Mo 3d and S 2p core levels, respectively, of 600 ^oC-, 800 ^oC-, and 1000 ^oC-MoS_2 nanosheets on Si. The Mo 3d spectra show three peaks at 232.5, 229.3, and 226.5 eV, which correspond to the Mo $3d_{3/2}$ and Mo $3d_{5/2}$ doublet state and the S 2s state, respectively. The S 2p core level spectra contain two peaks at 163.4 and 162.2 eV, which are assigned to the S $2p_{1/2}$ and S $2p_{3/2}$ doublet, respectively. The calculated stoichiometric ratio (S/Mo) is close to 2 (1.98 for 600 ^oC-MoS_2 and 1.95 for 800 ^oC- and 1000 ^oC-MoS_2), and all the XPS results agree with the previous reported results for MoS_2.[30] Additionally, the XPS survey spectra show that all three MoS_2 nanosheets samples have the same chemical compositions of molybdenum and sulfur elements, with little incorporation of carbon impurity from surface contamination (see Figure S2(a) in the Supporting Information).

The combined results of Raman and XPS analysis confirm that the as-prepared MoS_2 samples are comprised of stoichiometric MoS_2 nanosheets which increase in crystallinity as the annealing temperature increases. These films serve as the substrates for decoration by ZnO NCs. Therefore, onto 600 ^oC-, 800 ^oC-, and 1000 ^oC-MoS_2 nanosheets, we deposited ZnO by ALD for 10 to 150 cycles. The process for ZnO ALD on the MoS_2 was characterized by XPS. Figure 2(a) and 2(b) show XPS spectra of the Zn 2p and O 1s core level, respectively, for samples made by applying 10, 30, 50, and 150 ZnO ALD cycles on 1000 ^oC-MoS_2. In Figure 2(a), there are two main peaks near 1045 and 1022 eV, assigned to the Zn $2p_{1/2}$ and Zn $2p_{3/2}$ states of ZnO.[35] The O 1s spectrum shown in Figure 2(b) for MoS_2 is comprised of a single peak at 530.5 eV, corresponding to Mo–O. After ZnO ALD, a new peak at 529 eV is additionally observed which is associated with O^{2-} ions bonded to Zn^{2+}.[36] This assignment agrees with the O 1s peak position previously reported for chemical vapor deposited ZnO grown by diethylzinc (DEZ) and O_2.[37] As more ZnO is deposited, the Mo–O peak can be seen as a shoulder on the higher binding energy side of the Zn–O peak.

With increased ALD cycle numbers, the intensities of the two Zn peaks and the O peak grow, consistent with the formation of more Zn–O bonds and a thicker film. Because the average escape depth of photoelectrons in a ZnO film is less than 3 nm,[38] once a fully continuous ZnO film reaches a thickness above 3 nm, the intensity of Zn–O bonds detected in XPS would be expected to reach a steady state intensity and no longer increase. Given the ZnO ALD growth rate of 1.8 Å /cycle, this would be expected to occur by ~17 ALD cycles on a Si substrate. However, as seen in Figure 2(a), the Zn and O signal intensities in XPS for ZnO deposited on the MoS_2 substrate increase gradually up to 150 cycles. This observation indicates that the deposited ZnO film is either very thin or does not have continuous coverage on MoS_2 due to island growth. Thus, we propose that a significant nucleation delay of ALD ZnO on the MoS_2 nanosheet surface exists, in comparison to ALD on a typical substrate such as Si.[39]

Figure 2(c) shows the Zn 2p spectra after 30 cycles of ZnO ALD on 600 ^{o}C-, 800 ^{o}C-, and 1000 ^{o}C-MoS_2 nanosheets. Interestingly, the Zn signal intensity decreases with increased annealing temperature, which indicates that more ZnO is deposited on the MoS_2 films prepared at lower annealing temperatures. For a more quantitative comparison, the relative atomic percentages of Zn/(Zn + Mo) extracted from survey XPS spectra (see Supporting Information in Figure S2(b)-(d)) are plotted in Figure 2(d) as a function of increasing ZnO cycles on 600 ^{o}C-, 800 ^{o}C-, and 1000 ^{o}C-MoS_2 nanosheets. While ZnO ALD on all MoS_2 samples leads to a gradual increase of the amount of Zn on the surface, the rates of increase differ between the samples. The fastest increase in the Zn amount is observed for the 600 ^{o}C-MoS_2 sample, indicating that more ZnO is deposited on this sample, followed by the 800 ^{o}C-MoS_2 and then the 1000 ^{o}C-MoS_2 sample. For all three MoS_2 samples, the rate of increase gradually slows as the cycle number increases, finally achieving the saturation value of 100 at. % at 150 cycles. These results suggest that 150 cycles of ZnO are sufficient to cover the entire surface of MoS_2 independent of the MoS_2 annealing temperature. At the same time, the data in Figure 2(d) also indicate that ZnO does not form a continuous film until at least 50 cycles even for the fastest growing sample, consistent with the conclusion reached from Figure 2(a). Additionally, as the number of ZnO ALD cycles increases, a decrease in the intensity of Mo–S bonds is observed, as shown in Figure S2(e). This decrease is attributed to the increase in ZnO film thickness covering the MoS_2. Also, compared to bare MoS_2, the shoulder at higher binding energy than Mo–S bonds is observed after 10 cycles of ALD ZnO. It corresponds to Zn–

S bonds which would be attributed to the reaction of DEZ with MoS_2. This intensity of the shoulder decreases similar to Mo–S bonds indicating that Zn–S bonds mainly exist at the surface of MoS_2. Because ALD ZnO was performed on all of the MoS_2 substrates under the same process conditions, the different behaviors seen for ZnO uptake must arise solely from the different surface characteristics of the MoS_2 nanosheets depending on their annealing temperature.

Scanning Auger electron spectroscopy (AES) maps of 50 cycles ALD ZnO on MoS_2 reveal non-uniform growth of ZnO (see Figure S3 in Supporting Information), in contrast to the growth behavior of ZnO on Si observed by scanning electron microscopy (SEM) (see Figure S4 in Supporting Information). To understand the growth behavior of ZnO on MoS_2, the morphologies with increasing ZnO ALD cycle number are investigated by SEM. Figures 3(a), 3(b), and 3(c) show ALD ZnO after 10, 30, and 50 cycles (from left to right images) on 600 ^{o}C-, 800 ^{o}C-, and 1000 ^{o}C-MoS_2 nanosheets, respectively. SEM images of MoS_2 substrates before and after 150 ALD cycles are presented in Figure S5(a) and S5(b), respectively, in Supporting Information. The images show that after 10 cycles, ALD ZnO deposits on MoS_2 as small 0D ZnO particles. With increasing cycle number up to 50, the ZnO particles grow and they also branch out on the $MoS_{2,}$ expanding into a 1D dotted line shape, indicating that the 0D ZnO nuclei become interconnected along the 1D lines.

We believe that the behavior reflects the nucleation and growth of ZnO particles along MoS_2 grain boundaries for the following two reasons. First, the grain boundaries in 2D materials have been reported to be linearly-arranged intrinsic defects,[40,41] which was also observed in Figure 1(c). Second, in previous studies, ALD NCs were shown to selectively form on line defects of 2D materials such as grain boundaries due to the higher chemical reactivity at the defects than at the pristine sites.[40,42,43] Thus, we conclude from this work that ZnO islands nucleate along 1D grain boundaries in the MoS_2 and form 1D line shapes upon further ALD cycles. Notably, after 150 cycles, coalescence of the ZnO particles is observed, resulting in full coverage of ZnO on MoS_2 for all the MoS_2 surfaces studied (see Figure S5(b) in Supporting Information). However, differences in the deposited ZnO morphology are seen between the MoS_2 samples for some of the intermediate ALD cycle numbers. As evident in Figure 3, although the areal coverages of ALD ZnO after 10 cycles are not clearly distinguishable across three different MoS_2 surfaces, by 30 cycles of ALD ZnO, the areal coverage of ALD ZnO on 1000 ^{o}C-MoS_2 is apparently much smaller than that on 600 ^{o}C-MoS_2.

For quantitative analysis, the areal coverage and number density of ZnO NCs at various ZnO ALD cycle numbers determined from the SEM images are plotted in Figures 3(d) and 3(e), respectively. As shown in Figure 3(d), higher areal ZnO coverages are observed on the MoS_2 prepared at a lower annealing temperature for ALD cycles up to 50, consistent with the observation by XPS shown in Figure 2. By 150 cycles, the areal coverage of ZnO reaches ~100% for all the samples, evident in the SEM images of Figure S5(b). For comparison, the areal coverages of ZnO on MoS_2 are much smaller than those on Si for all ALD cycle numbers studied,[39] with SEM images showing that the ZnO morphologies at even 10 and 30 cycles on Si are flat and smooth (see Figure S4 in Supporting Information). Because the density of reactive sites such as −OH groups for ALD nucleation on a Si surface is much greater than the density of defect sites on MoS_2, the nucleation rate is expected to be higher on Si than on MoS_2, leading to high surface coverage.

For all MoS_2 samples, the number density of ZnO particles shown in Figure 3(e) gradually increases, then decreases after a certain number of cycles due to the coalescence of nuclei. Although there is uncertainty in the exact cycle number, the data in Figure 3(e) show that coalescence begins at around 30 cycles for all three MoS_2 samples. The areal nucleation rate of

ALD ZnO, which is defined as the number of nuclei per ALD cycle per area, can be estimated from the initial slope of the number density plot because we assume that prior to coalescence, each particle represents a nucleus. The resulting rates of ALD ZnO during the initial 10 cycles are 1.39, 1.16, and 1.04 × 10^9/cm^2·cycle for 600 ^{o}C-, 800 ^{o}C- and 1000 ^{o}C-MoS_2. Note that the slope of the number density plot after 30 cycles does not represent the areal nucleation rate of ZnO because the population of particles observed at that point are dominated by NCs formed from coalescence. Since the only difference between these experiments was the preparation condition of the MoS_2 substrate, we conclude that the different nucleation rates of ZnO ALD on MoS_2 correspond to the following reactivity trend of the as-prepared MoS_2 surfaces: 600 ^{o}C-MoS_2 > 800 ^{o}C-MoS_2 > 1000 ^{o}C-MoS_2. Moreover, the maximum number density of ZnO particle (reached at 30 cycles in Figure 3(e)) can be used as an estimate of the lower limit of the density of nucleation sites on MoS_2 (a lower limit because it is likely that some of the nuclei have already begun coalescing by 30 cycles); these values indicate that the nucleation site density decreases with increased MoS_2 annealing temperature. Thus, the higher areal coverage of ALD ZnO on 600 °C-MoS_2 is attributed to a higher density of nucleation sites at the MoS_2 surface.

While SEM measurements are widely used to evaluate surface morphologies of nanomaterials, SEM cannot easily provide some of the information about NC morphology such as average size with varying cycle numbers, due to its limited spatial resolution and probe area. Hence, to further quantify the average sizes of ZnO nuclei, grazing incidence small angle X-ray scattering (GISAXS) techniques are employed. Representative GISAXS patterns of Si and of 1000 ^{o}C-MoS_2 on Si are shown in Figure 4(a) and 4(b), respectively, and those of 600 ^{o}C- and 800 ^{o}C-MoS_2 on Si are shown in Figure S6(a) and S6(b) in Supporting Information, respectively. Qualitatively, these GISAXS data confirm the presence of smooth and thin MoS_2 nanosheets on the Si substrates.

The position of the Yoneda peak ($\alpha_f = \alpha_c$) typically corresponds to the weighted critical angle (α_c) of the substrate and the deposited materials, which allows for tracking of the deposition process. For Si, a weak diffuse scattering signal is observed in Figure 4(a) along the Yoneda peak denoted by the red arrow, matching the critical angle of Si ($\alpha_c = 0.18°$ at 10.0 keV X-rays). For MoS_2 nanosheets on Si (Figure 4(b)), scattered X-rays denoted by the white solid arrow are found to locate mainly along the vertical direction ($2\theta_f = 0°$), which also indicates that the deposited MoS_2 nanosheets have uniform and smooth surfaces. Additionally, the film fringes indicated by the white dashed arrow in Figure 4(b) can be used to estimate the thickness of MoS_2 nanosheets, *h*, where $h \approx 2\pi/\Delta Q_z$ and ΔQ_z is the difference between the two intensity minima along the vertical direction ($2\theta_f = 0°$), after converting the images into reciprocal space.[44] The estimated thicknesses of MoS_2 nanosheets on Si from this analysis are ~3.1, 4.4 and 3.9 nm for 600 °C-, 800 °C-, and 1000 °C-MoS_2, respectively, which are consistent with the observations by Raman and TEM analysis. The GISAXS patterns of the samples after 10, 30, 50 and 150 ALD cycles of ZnO on 1000 °C-MoS_2 nanosheets are shown in Figure 4(c)-4(f), and those on 600 °C- and 800 °C-MoS_2 are in Figure S6(c)-(f) and Figure S6(g)-(j) in Supporting Information, respectively. For all three MoS_2 samples, the Yoneda peak gradually shifts from 0.18° to 0.25° with increasing ZnO ALD cycle number, which indicates the formation of ZnO NCs, since $\alpha_c = 0.27°$ for ZnO with 10.0 keV X-rays.

To produce a more quantitative analysis of the GISAXS data, the data were fitted using a model in which each ZnO nucleus possesses a spheroid shape. The extracted average lateral radius, defined as the half of diameter (*D*) value, of ZnO nuclei on 600 °C-, 800 °C-, and 1000 °C-MoS_2 are plotted in Figure 4(g) for 10, 30, 50, and 150 cycles. More dimensional information (*D* and height (*H*)) is summarized in Table S1 in Supporting Information. The average lateral radius of the ZnO nuclei on MoS_2 shows a continuous increase, finally reaching ~8 nm at 150 cycles. Within the uncertainty of the data, the radii of ZnO NCs are the same for the 600 °C-, 800 °C-, and 1000 °C-MoS_2 samples at each number of ALD cycles studied. The similarity in the sizes of the ZnO NCs on the three MoS_2 nanosheets with increasing ALD cycle numbers is consistent with expectation, since once the ZnO nuclei form at defect sites on the MoS_2 nanosheets, the steady state ZnO growth rate on these nuclei should ideally be constant under the same process condition. On the other hand, deviations in the radii across the three samples should arise if the onset of coalescence differs significantly between them, since a NC comprised of a group of coalesced islands will have a larger radius. However, such an effect is not observed, suggesting that all three samples experience coalescence at a similar number of ALD cycles. In fact, this is what is observed in Figure 3(e), in which the nuclei number density peaks at 30 ALD cycles for all samples. Also informative is the asymptotic approach to a constant lateral radius value for all three MoS_2 samples by 150 ALD cycles. Considering that the areal coverage increases to 100% by 150 cycles (Figure 3(d)), the data indicate that at this point in the ALD process, the ZnO NCs can’t get any larger because the surface is fully covered and the NCs abut one another.

The crystalline structure of the ZnO NCs on MoS_2 is also probed by employing the GIWAXS techniques. The GIWAXS patterns obtained from the 600 °C-, 800 °C-, and 1000 °C-MoS_2 nanosheets are shown in Figure 4(h). By matching the crystalline peak positions, the data indicate that the hexagonal 2H-MoS_2 phase is formed for all three annealing temperatures, as the *d*-spacings correspond to the major (002) peaks for 2H-MoS_2 at a Q value of 1.0 $Å^{-1}$ in the out-of-plane direction. The broad peak located at Q = 1.5 $Å^{-1}$ corresponds to amorphous SiO_2 diffraction. The GIWAXS patterns collected for ZnO on the 800 °C-MoS_2 nanosheets are shown in Figure 4(i), and those on 600 °C- and 1000 °C-MoS_2 are shown in Figure S7(a) and S7(b) in Supporting Information, respectively. In addition to the crystalline MoS_2 diffraction peaks, three major peaks located between Q = 2.2 Å $^{-1}$ and 2.6 Å $^{-1}$, corresponding to the ZnO (010), (002), and (011) diffraction peaks, are seen for the 50 and 150 ALD cycle samples. These peaks are observed on all three types of MoS_2 substrates, and in each case the 150 cycle samples have a much higher intensity compared to the 50 cycle samples. The domain sizes of ZnO, *B*, for all 150 cycle films are estimated to be ~6.4 nm according to the Scherrer equation ($B = 1.8\pi/\Delta Q$). Note that this value represents the average single crystal grain size, even though the NCs coalesce. Since it is smaller than the average diameter of ZnO NCs, 16.5~17.4 nm at 150 cycles shown in Table S1, we conclude that most ZnO NCs are composed of several single crystal grains of ZnO. Meanwhile, the preferred orientation of ZnO NCs with respect to the basal plane of the MoS_2 might have profound implications on the nucleation behavior since the (100) surface is charge neutral and the (002) surface is a charged plane. However, as shown in a 2D GIWAXS image in Figure S7(c), there is no notably preferred orientation with respect to the MoS_2 planes.

To complement the investigation of nucleation and growth mechanisms of ALD ZnO on MoS_2, the adsorption of the DEZ precursor on the basal plane and edge site of MoS_2 is calculated by density functional theory (DFT), and the results are shown in Figure 5. The reaction pathways of the basal plane *versus* S-edge site toward dissociative adsorption of DEZ into ethyl and ethylzinc moieties are compared. Molecular adsorption of DEZ exhibits a small exothermicity of ca. -0.7 eV for both basal plane and edge sites at the intermediate state, as is typical for a physisorption configuration. On the other hand, while dissociative adsorption of DEZ on the MoS_2 edge site involves only a small barrier of 0.15 eV and provides further stabilization compared to molecular adsorption, the same reaction step on the basal plane faces a larger activation energy of 0.94 eV and is endothermic. Thus, the DFT calculation results show that adsorption of the DEZ precursor is unfavorable on the basal plane of MoS_2, but will occur spontaneously on the defect sites, corresponding to the first step in growth of ZnO.

These results are consistent with the experimental observation that the nucleation rate of ZnO NCs can be varied by the defect density at the MoS_2 surface, which in turn can be controlled by the MoS_2 preparation conditions. By the Raman results in Figure 1(b), we observe that the structural quality of MoS_2 related to crystallinity and grain size is improved at elevated annealing-temperature of the MoS_2 substrate. It is well known that the reactivity of the basal planes of MoS_2 is much smaller than that of defective sites such as edges,[45,46] as supported by the current DFT results. Taken together, these results indicate that the surface density of grain boundaries, which are the main nucleation sites for ZnO on the MoS_2 surface, is larger for the 600 ^oC-MoS_2 sample compared to the 1000 ^oC-MoS_2 sample, which has larger grains. Hence, nucleation will occur more readily on MoS_2 surfaces that are annealed to a lower temperature and have a higher density of defects. The amount of deposited ZnO as determined by the XPS results in Figure 2 increases as the annealing temperature of MoS_2 decreases, consistent with this analysis. The density of nucleation defects on the MoS_2 surface also influences the morphology of the deposited ZnO. Since the grain boundaries of MoS_2 are mostly composed of linear arrangements of defects, 1D ZnO can grow selectively by connecting 0D ZnO NCs that nucleate along the grain boundaries, as observed in the SEM images of Figure 3.

Meanwhile, although the DEZ adsorbs predominantly at defect sites, there still exists the possibility of growth on pristine basal plane sites. Previous studies of ALD of metal oxides on MoS_2 suggested physisorption of the metal precursor as the first step leading to film deposition.[47-49] However, the low physisorption energy of small-sized metal precursors such as DEZ (intermediate energy calculated in Figure 5), suggests a low nucleation density on the basal plane.

In contrast, the spontaneous dissociative chemisorption of DEZ predicted by DFT calculations to occur on defect sites would allow more facile nucleation of ZnO. This prediction from DFT is consistent with the SEM images, which show interconnected ZnO NCs that appear to follow grain boundaries.

Because the growth mechanism favors nucleation of ZnO NCs at defect sites on MoS_2, and because that defect site density can be controlled by varying the preparation conditions of the MoS_2, the process provides an opportunity to create controlled hybrid nanostructures. To this end, we improved the surface-to-volume ratio of a hybrid nanostructure by employing vertical NWs of 3D MoS_2 as a substrate for decorating by 0D ZnO NCs. Figure 6(a) shows an SEM image of as-synthesized MoS_2 NWs prepared by sulfurization of MoO_3 on SiO_2/Si NWs at 800 ℃. The NWs are arranged as freestanding features with an average height of 10 μm and diameter of 400 nm. Figure 6(b) shows Mo (left) and S (right) elemental mapping images measured by Energy-dispersive X-ray spectroscopy (EDS) taken as a top-view of the MoS_2 NWs, with the inset in the left image in Figure 6(b) showing a top view SEM image. The chemical composition analysis shows both Mo and S signals are randomly distributed over the top-surface of the NWs. Figure 6(c) shows an SEM image of 3D MoS_2 NWs after depositing 0D ZnO NCs with 30 ALD cycles. On the surface of the 3D MoS_2 NWs, small ZnO NCs are observed as connected segments, similar to what was observed on the 2D MoS_2 nanosheets shown in Figure 3. In addition, isolated 0D ZnO NCs are also seen on the MoS_2 NW surface, which may be caused by the existence of 0D surface defects sites far from the grain boundaries present on the NWs, shown in the inset of Figure 6(c).

Figure 6(d) and 6(e) show cross-sectional, atomic scale HR-STEM images for vertical and horizontal directions along the NWs, respectively (other views are presented in Figure S8 in Supporting Information). Spheroid-shaped features associated with the ALD ZnO NCs can be seen adsorbed on the MoS_2 NWs, most clearly observed in the right image of Figure 6(d) and in Figure 6(e). The average diameter of the ZnO NCs after 30 cycles ALD ZnO on 800 ℃-MoS_2 seen in the HR-STEM images is 5~7 nm, consistent with the results measured by GISAXS shown in Table S1.

The crystalline structure of the ZnO NCs on MoS_2 NWs is obtained by fast Fourier transform (FFT), shown in Figure 6(f), from the entire image of Figure 6(e). There are three notable peaks, assigned to MoS_2 (002) together with ZnO (010) and (011), corresponding to the crystalline patterns observed from GIWAXS shown in Figure 4(i). The left-side images in Figures 6(g) and 6(h) are magnified HR-STEM images, and the right-side images are the corresponding FFT patterns, both from the A and B regions in Figure 6(e), respectively. From the magnified HR-STEM images, the *d*-spacing values of ZnO obtained were 2.48 Å and 2.81 Å for ZnO in Figure 6(g) and 6(h), respectively. Matching these values with the JCPDS card reveal that they correspond to ZnO (010) and (011), respectively, in agreement with the FFT and GIWAXS analysis. These preferred orientations of (010) and (011) agree with previous observation obtained from ZnO grown below 200 ℃.[50] The hybrid material synthesis method introduced here and the improved understanding of its nucleation and growth mechanisms may help guide the fabrication of functional MoS_2-based electronic devices.

CONCLUSIONS

We investigate the growth characteristics of ZnO on MoS_2 and successfully achieve morphological engineering of ZnO/MoS_2 hybrid structures through variations in the crystallinity and dimensionality of the MoS_2 substrate and tuning of the concentration and size of ZnO NCs.

The morphologies can be systematically controlled by changing the sulfurization temperature used to form the MoS_2 and by varying the number of cycles of ZnO ALD. We elucidate a growth mechanism in which selective nucleation of 0D NCs of ZnO occurs at defect sites on the MoS_2 at low cycle numbers, followed by a rise in areal coverage and nucleus size with increasing ALD cycle number, finally resulting in coalescence by neighboring 0D NCs at high cycle numbers. Importantly, larger grains with fewer grain boundaries of MoS_2 are obtained when the MoS_2 is prepared at higher temperatures, resulting in a low concentration of ZnO NCs due to fewer reactive nucleation sites. The sizes of the ZnO nuclei are similar for the three MoS_2 surfaces studied, independent of the defect density of MoS_2. At the highest cycle numbers, the coverage of NCs on the MoS_2 surface increases, with the NCs approaching a limiting average lateral radius of ca. 8 nm. The surface reaction of the DEZ molecule on MoS_2 is analyzed using quantum chemical calculations, showing that spontaneous dissociative chemisorption of the DEZ precursor on defect sites allows nucleation of ZnO, rendering the morphologies of the hybrids tunable by controlling the number of defects on MoS_2. The results of this combined experimental and theoretical study are expected to inform fundamental understanding of nucleation and growth mechanism of NCs on TMDCs and should significantly expand the applications of TMDC nanostructures.

METHODS

Substrates and MoS_2 Synthesis Methods. The MoS_2 samples were made by depositing MoO_3 films on either crystalline Si samples or SiO_2/Si NWs, then sulfurizing them in H_2S. A commercial 6-inch ALD chamber (Plus 150, Quros) containing a loadlocked chamber was used for the deposition of the MoO_3 films. The films were deposited on Si (100) substrates by plasma-enhanced ALD (PE-ALD) using $Mo(CO)_6$ and O_2 plasma at a 200 ℃ growth temperature after cleaning the substrates in RCA solution (1:1:5 $NH_4OH/H_2O_2/H_2O$ by volume) at 70 ℃ for 10 min, followed by dipping in buffered oxide enchant solution for 30 s to remove native oxide. The temperature of the bubbler containing $Mo(CO)_6$ was maintained at 35 ℃ to produce adequate vapor pressure. Vaporized $Mo(CO)_6$ molecules were transported into the chamber by pure Ar (99.999%) carrier gas, of which flow was controlled by mass flow controller (MFC). The O_2 flow and plasma power were fixed at 300 sccm and 200 W, respectively. A MoO_3 ALD cycle consisted of four steps: 5 s of $Mo(CO)_6$ precursor exposure, 12 s of Ar purging, 5 s of O_2 plasma reactant exposure and another 12 s of Ar purging, leading to a growth rate of 1.2 Å /cycle.

For the sulfurization, we used a home-made furnace[29] specifically designed for high-temperature annealing. MoO_3 samples were annealed with a two-step process: initially, the samples were heated to 200 ℃ from room temperature (RT) and held for 60 min. Subsequently, the temperature was gradually increased from 200 ℃ to the desired annealing temperatures of 600, 800, or 1000 ℃ at 13.3 ℃/min for the sulfurization of MoO_3. Samples were kept at each peak temperature for 60 min, and then cooled down. In the process of annealing, the Ar (50 sccm) and H_2S (5 sccm) were flowed continuously before cooling began, then only Ar (50 sccm) gas was flowed when cooling to RT. The MoS_2 samples prepared at 600, 800, and 1000 ℃ will be abbreviated as 600 ℃-, 800 ℃-, and 1000 ℃-MoS_2, respectively.

Both MoS_2 2D nanosheets and 3D NWs were fabricated. The MoS_2 2D nanosheets were prepared on planar Si (100). The 3D NWs were made by performing the MoO_3 deposition on thermally oxidized Si NWs substrates and subsequent sulfurization, using the following process. Aligned Si NWs were fabricated by a gold-assisted chemical etching method[51] and oxidized in O_2 ambient (0.6 Torr) at 1000 ℃ for 1 h to form a SiO_2 layer on the Si NWs surface. A MoO_3 film of 50 cycles (thickness ~6 nm) was deposited by PE-ALD on the SiO_2/Si NWs which have a diameter of 400 nm and a length of 10 μm. Subsequently, $MoO_3/SiO_2/Si$ NWs were sulfurized to form $MoS_2/SiO_2/Si$ NWs arrays at 800 ℃. Details of the ALD and sulfurization process configuration were presented in our previous work on the fabrication of WSe_2 nanotubes.[29]

ZnO ALD. A commercial ALD reactor (GEMStar-6 reactor, Arradiance, Inc.) was utilized for ZnO ALD using DEZ (Sigma-Aldrich) and H_2O as the precursor and counter reactant, respectively. One cycle of ZnO ALD included 30 ms for DEZ and H_2O exposure, and 10 s for the nitrogen purge between each pulse, and films were deposited at 150 ℃. Under these ALD conditions, ZnO deposition exhibited linear growth characteristics with a growth rate of 1.8 Å /cycle. After the ZnO growth, samples were removed from the reactor for *ex-situ* characterization and analyses.

Characterization. The number of MoS_2 layers and their structural quality were analyzed by Raman spectroscopy (HORIBA, Lab Ram ARAMIS; 532-nm laser excitation wavelength). The elemental composition and chemical bonding structure were analyzed by XPS (PHI VersaProbe) microprobe using an Al Kα monochromatic source of 1486.6 eV. The surface morphology of the films was analyzed by plan-view observation with SEM (FEI Magellan 400 XHR). EDS was performed using an SEM equipped with a XFlash 630 detector for elemental mapping of ZnO/MoS_2 surface. The surface coverage of ZnO was calculated from the planar SEM images using ImageJ software. To count the number of ZnO particles and measure their size, we changed the SEM image into a binary, black and white, image with an automatic-threshold setting in the ImageJ program. This allows the ZnO particles to be distinguished from the MoS_2 substrate so that the software can count the number of particles and their average size. The 2D elemental mapping and chemical compositions were further carried out by AES (PHI 700 Field Emission Scanning Auger Nanoprobe). The atomic structure of 2D MoS_2 nanosheets and hybrid 3D nanostructures was explored by STEM (FEI Titan 80-300) which was operated at an accelerating voltage of 80 kV. Each sample of 2D MoS_2 nanosheets and hybrid 3D nanostructures was transferred onto a TEM grid using the conventional wet transfer method[52] as polymethyl methacrylate (PMMA) is coated onto the MoS_2 as a film support and the composite stack is separated from the substrate using chemical etching.

The microstructures of the films were analyzed by GISAXS at Beamline (BL) 1-5 at the Stanford Synchrotron Radiation Lightsource (SSRL). For the GISAXS measurements, 10 keV X-rays were shined on the samples with a 0.6° incident angle. The beam center position and the distance between sample and detector were calibrated by using silver behenate with an Igor-based Nika software.[53] The calibrated images were analyzed using FitGISAXS software[44] to extract the particle D and H by fitting the horizontal line-cut along the Yoneda peak.[54] To investigate crystalline structures, GIWAXS was also performed at BL 11-3 at the SSRL. The GIWAXS data were collected by a MAR345 2D imaging detector using a 12.7 keV X-ray source with an incident angle of 0.5°. The detector was ~150 mm away from the sample, and the position was calibrated using a LaB_6 reference and the WxDiff software package.[55]

Quantum Chemical Calculation. DFT calculations were carried out with the Quantum Espresso package[56] using the PBE functional,[57] semi-empirical Grimme's D2 dispersion correction for van der Waals interactions,[58] projector augmented-wave method,[59] and an energy cutoff of 450 eV. All atoms were allowed to relax until residual forces became smaller than 0.02 eV/Å . For the (002) basal plane, a (4×4) area of monolayer of 2H MoS_2 slab was considered with a (5×5×1) Monkhorst-Pack k-point mesh. Each slab was separated for more than 15 Å in the vertical direction to minimize the neighboring interactions. Using this method, an in-plane lattice constant of MoS_2 of a = 3.22 Å could be obtained. In addition, a 50%-S-edge[60] monolayer slab with a (4×4) area behind the edge was considered, which was separated for more than 15 Å in lateral direction as well. For the S-edge slab, a (1×5×1) Monkhorst-Pack *k*-point mesh was used. The transition states were located using the climbing image-nudged elastic band (CI-NEB) method.[61]

ASSOCIATED CONTENT

Supporting Information. The Supporting Information is available free of charge *via* the Internet at http://pubs.acs.org.

GIWAXS images of MoS_2 (Figure S1), XPS spectra of MoS_2 and ZnO on MoS_2 (Figure S2), SEM images and AES maps of ZnO on MoS_2 (Figure S3), SEM images of ZnO on Si (Figure S4), SEM images of MoS_2 before and after 150 cycles ZnO (Figure S5), GISAXS patterns of MoS_2 and ZnO on MoS_2 (Figure S6), D and H values of ZnO on MoS_2 (Table S1), GIWAXS patterns of ZnO on MoS_2 (Figure S7), and SEM and STEM images of ZnO on MoS_2 NWs (Figure S8) are supplied as Supporting Information. The following file is available free of charge. Supporting information (PDF)

AUTHOR INFORMATION

Corresponding Author

*Corresponding author's email: sbent@stanford.edu

Author Contributions

#These authors contributed equally to this work.

ACKNOWLEDGMENTS

This work was supported by the Department of Energy under Award Number DE-SC0004782, including ZnO ALD, X-ray techniques, and characterization and testing of ZnO/MoS_2. The MoS_2 synthesis carried out by W.-H.K. was supported by the National Research Foundation of Korea (NRF) grant funded by the Korea government (MSIP) (No. NRF-2017R1C1B5076821), the Ministry of Trade, Industry & Energy (MOTIE) (No. 20006504), and the Korea Semiconductor Research Consortium (KSRC) support program for the development of the future semiconductor device. The theoretical calculations carried out by B.S. was supported by a National Research Foundation of Korea (NRF) grant funded by the Korea government (MSIT) (NRF-2019R1F1A1058615). A.J.M.M. was supported by the Netherlands Organization for Scientific Research (NOW-Rubicon 680-50-1309) for a postdoctoral fellowship. D.B. was supported by the LEaDing Fellowship grant from the European Union's Horizon 2020 research and Innovation Programme under the Marie Sklodowska-Curie grant agreement no. 707404. Part of this work was performed at the Stanford Nano Shared Facilities (SNSF) supported by the National Science Foundation under award ECCS-1542152, and GISXAS and GIWAXS were performed at the SSRL.

REFERENCES

(1) Li, H.; Yin, Z.; He, Q.; Li, H.; Huang, X.; Lu, G.; Fam, D. W. H.; Tok, A. I. Y.; Zhang, Q.; Zhang, H. Fabrication of Single- and Multilayer MoS_2 Film-Based Field-Effect Transistors for Sensing NO at Room Temperature. *Small* **2012**, *8*, 63–67.

(2) Voiry, D.; Salehi, M.; Silva, R.; Fujita, T.; Chen, M.; Asefa, T.; Shenoy, V. B.; Eda, G.; Chhowalla, M. Conducting MoS_2 Nanosheets as Catalysts for Hydrogen Evolution Reaction. *Nano Lett.* **2013**, *13*, 6222–6227.

(3) Tao, L.; Long, H.; Zhou, B.; Yu, S. F.; Lau, S. P.; Chai, Y.; Fung, K. H.; Tsang, Y. H.; Yao, J.; Xu, D. Preparation and Characterization of Few-Layer MoS_2 Nanosheets and Their Good Nonlinear Optical Responses in the PMMA Matrix. *Nanoscale* **2014**, *6*, 9713–9719.

(4) Chang, K.; Chen, W. L-Cysteine-Assisted Synthesis of Layered MoS_2/Graphene Composites with Excellent Electrochemical Performances for Lithium Ion Batteries. *ACS Nano* **2011**, *5*, 4720–4728.

(5) Radisavljevic, B.; Radenovic, A.; Brivio, J.; Giacometti, V.; Kis, A. Single-Layer MoS_2 Transistors. *Nat. Nanotechnol.* **2011**, *6*, 147–150.

(6) Huang, X.; Zeng, Z.; Bao, S.; Wang, M.; Qi, X.; Fan, Z.; Zhang, H. Solution-Phase Epitaxial Growth of Noble Metal Nanostructures on Dispersible Single-Layer Molybdenum Disulfide Nanosheets. *Nat. Commun.* **2013**, *4*, 1444–1448.

(7) Zhai, C.; Zhu, M.; Bin, D.; Ren, F.; Wang, C.; Yang, P.; Du, Y. Two Dimensional MoS_2/Graphene Composites as Promising Supports for Pt Electrocatalysts towards Methanol Oxidation. *J. Power Sources* **2015**, *275*, 483–488.

(8) Shi, Y.; Huang, J. K.; Jin, L.; Hsu, Y. Te; Yu, S. F.; Li, L. J.; Yang, H. Y. Selective Decoration of Au Nanoparticles on Monolayer MoS_2 Single Crystals. *Sci. Rep.* **2013**, *3*, 1–7.

(9) Zhou, W.; Yin, Z.; Du, Y.; Huang, X.; Zeng, Z.; Fan, Z.; Liu, H.; Wang, J.; Zhang, H. Synthesis of Few-Layer MoS_2 Nanosheet-Coated TiO_2 Nanobelt Heterostructures for Enhanced Photocatalytic Activities. *Small* **2013**, *9*, 140–147.

(10) Zhao, Y. F.; Yang, Z. Y.; Zhang, Y. X.; Jing, L.; Guo, X.; Ke, Z.; Hu, P.; Wang, G.; Yan, Y. M.; Sun, K. N. Cu_2O Decorated with Cocatalyst MoS_2 for Solar Hydrogen Production with Enhanced Efficiency under Visible Light. *J. Phys. Chem. C* **2014**, *118*, 14238–14245.

(11) Lim, S. K.; Hwang, S. H.; Kim, S.; Park, H. Preparation of ZnO Nanorods by Microemulsion Synthesis and Their Application as a CO Gas Sensor. *Sens. Actuators, B* **2011**, *160*, 94–98.

(12) Gao, X.; Zhao, H.; Wang, J.; Su, X.; Xiao, F. Morphological Evolution of Flower-Like ZnO Microstructures and Their Gas Sensing Properties. *Ceram. Int.* **2013**, *39*, 8629–8632.

(13) Guo, J.; Peng, C. Synthesis of ZnO Nanoparticles with a Novel Combustion Method and Their C_2H_5OH Gas Sensing Properties. *Ceram. Int.* **2015**, *41*, 2180–2186.

(14) Fan, F.; Tang, P.; Wang, Y.; Feng, Y.; Chen, A.; Luo, R.; Li, D. Facile Synthesis and Gas Sensing Properties of Tubular Hierarchical ZnO Self-Assembled by Porous Nanosheets. *Sens. Actuators, B* **2015**, *215*, 231–240.

(15) Sun, Z.; Chang, H. Graphene and Graphene-Like Two-Dimensional Materials in Photodetection: Mechanisms and Methodology. *ACS Nano* **2014**, *8*, 4133–4156.

(16) Li, J.; Yu, K.; Tan, Y.; Fu, H.; Zhang, Q.; Cong, W.; Song, C.; Yin, H.; Zhu, Z. Facile Synthesis of Novel MoS_2@SnO_2 Hetero-Nanoflowers and Enhanced Photocatalysis and Field-Emission Properties. *Dalton. Trans.* **2014**, *43*, 13136–13144.

(17) Yu, J.; Yu, X. Hydrothermal Synthesis and Photocatalytic Activity of Zinc Oxide Hollow Spheres. *Environ. Sci. Technol.* **2008**, *42*, 4902–4907.

(18) Feng, J.-J.; Liao, Q.-C.; Wang, A.-J.; Chen, J.-R. Mannite Supported Hydrothermal Synthesis of Hollow Flower-Like ZnO Structures for Photocatalytic Applications. *CrystEngComm* **2011**, *13*, 4202–4210.

(19) Ahmad, M.; Yingying, S.; Nisar, A.; Sun, H.; Shen, W.; Wei, M.; Zhu, J. Synthesis of Hierarchical Flower-Like ZnO Nanostructures and Their Functionalization by Au Nanoparticles for Improved Photocatalytic and High Performance Li-Ion Battery Anodes. *J. Mater. Chem.* **2011**, *21*, 7723–7729.

(20) Yan, H.; Song, P.; Zhang, S.; Yang, Z.; Wang, Q. Facile Synthesis, Characterization and Gas Sensing Performance of ZnO Nanoparticles-Coated MoS_2 Nanosheets. *J. Alloys Compd.* **2016**, *662*, 118–125.

(21) Tan, Y. H.; Yu, K.; Li, J. Z.; Fu, H.; Zhu, Z. Q. MoS_2@ZnO Nano-Heterojunctions with Enhanced Photocatalysis and Field Emission Properties. *J. Appl. Phys.* **2014**, *116*, 064305.

(22) Liu, X.; Zhang, Y.; Liu, Q.; He, J.; Chen, L.; Li, K.; Jia, F.; Zeng, Y.; Lu, Y.; Yu, W.; Zhu, D.; Liu, W.; Wu, J.; He, Z.; Ang, K.-W. Band Alignment of ZnO/Multilayer MoS_2 Interface Determined by X-Ray Photoelectron Spectroscopy. *Appl. Phys. Lett.* **2016**, *109*, 071602.

(23) Walter, T. N.; Lee, S.; Zhang, X.; Chubarov, M.; Redwing, J. M.; Jackson, T. N.; Mohney, S. E. Atomic Layer Deposition of ZnO on MoS_2 and WSe_2. *Appl. Surf. Sci.* **2019**, *480*, 43–51.

(24) Kang, M. A.; Kim, S.; Jeon, I. S.; Lim, Y. R.; Park, C. Y.; Song, W.; Lee, S. S.; Lim, J.; An, K. S.; Myung, S. Highly Efficient and Flexible Photodetector Based on MoS_2-ZnO Heterostructures. *RSC Adv.* **2019**, *9*, 19707–19711.

(25) Jian, W.; Cheng, X.; Huang, Y.; You, Y.; Zhou, R.; Sun, T.; Xu, J. Arrays of ZnO/MoS_2 Nanocables and MoS_2 Nanotubes with Phase Engineering for Bifunctional Photoelectrochemical and Electrochemical Water Splitting. *Chem. Eng. J.* **2017**, *328*, 474–483.

(26) Liu, S.; Yu, B.; Zhang, H.; Fei, T.; Zhang, T. Enhancing NO_2 Gas Sensing Performances at Room Temperature Based on Reduced Graphene Oxide-ZnO Nanoparticles Hybrids. *Sens. Actuators, B* **2014**, *202*, 272–278.

(27) Zhang, H.; Feng, J.; Fei, T.; Liu, S.; Zhang, T. SnO_2 Nanoparticles-Reduced Graphene Oxide Nanocomposites for NO_2 Sensing at Low Operating Temperature. *Sens. Actuators, B* **2014**, *190*, 472–478.

(28) Kim, H. G.; Lee, H. B. R. Atomic Layer Deposition on 2D Materials. *Chem. Mater.* **2017**, *29*, 3809–3826.

(29) Song, J. G.; Park, J.; Lee, W.; Choi, T.; Jung, H.; Lee, C. W.; Hwang, S. H.; Myoung, J. M.; Jung, J. H.; Kim, S. H.; Lansalot-Matras, C.; Kim, H. Layer-Controlled, Wafer-Scale,

and Conformal Synthesis of Tungsten Disulfide Nanosheets Using Atomic Layer Deposition. *ACS Nano* **2013**, *7*, 11333–11340.

(30) Song, J. G.; Ryu, G. H.; Lee, S. J.; Sim, S.; Lee, C. W.; Choi, T.; Jung, H.; Kim, Y.; Lee, Z.; Myoung, J. M.; Dussarrat, C.; Lansalot-Matras, C.; Park, J.; Choi, H.; Kim, H. Controllable Synthesis of Molybdenum Tungsten Disulfide Alloy for Vertically Composition-Controlled Multilayer. *Nat. Commun.* **2015**, *6*, 1–10.

(31) Terrones, H.; Del Corro, E.; Feng, S.; Poumirol, J. M.; Rhodes, D.; Smirnov, D.; Pradhan, N. R.; Lin, Z.; Nguyen, M. A. T.; Elías, A. L.; Mallouk, T. E.; Balicas, L.; Pimenta, M. A.; Terrones, M. New First Order Raman-Active Modes in Few Layered Transition Metal Dichalcogenides. *Sci. Rep.* **2014**, *4*, 1–9.

(32) Comini, E.; Faglia, G.; Sberveglieri, G.; Pan, Z.; Wang, Z. L. Stable and Highly Sensitive Gas Sensors Based on Semiconducting Oxide Nanobelts. *Appl. Phys. Lett.* **2002**, *81*, 1869–1871.

(33) Kite, S. V.; Chate, P. A.; Garadkar, K. M.; Sathe, D. J. Effect of Annealing Temperature on Properties of Molybdenum Disulfide Thin Films. *J. Mater. Sci. Mater. Electron.* **2017**, *28*, 16148–16154.

(34) Reyes-Gasga, J.; Tehuacanero, S.; Yacamán, M. J. Moire Patterns in High Resolution Electron Microscopy Images of MoS_2. *Microsc. Res. Tech.* **1998**, *40*, 2–9.

(35) Hsieh, P. T.; Chen, Y. C.; Kao, K. S.; Wang, C. M. Luminescence Mechanism of ZnO Thin Film Investigated by XPS Measurement. *Appl. Phys. A: Mater. Sci. Process.* **2008**, *90*, 317–321.

(36) Chen, M.; Wang, X.; Yu, Y. H.; Pei, Z. L.; Bai, X. D.; Sun, C.; Huang, R. F.; Wen, L. S. X-Ray Photoelectron Spectroscopy and Auger Electron Spectroscopy Studies of Al-Doped ZnO Films. *Appl. Surf. Sci.* **2000**, *158*, 134–140.

(37) Zhang, Y.; Du, G.; Wang, X.; Li, W.; Yang, X.; Ma, Y.; Zhao, B.; Yang, H.; Liu, D.; Yang, S. X-Ray Photoelectron Spectroscopy Study of ZnO Films Grown by Metal-Organic Chemical Vapor Deposition. *J. Cryst. Growth* **2003**, *252*, 180–183.

(38) Zemek, J.; Hucek, S.; Jablonski, A.; Tilinin, I. S. Photoelectron Escape Depth. *J. Electron Spectrosc. Relat. Phenom.* **1995**, *76*, 443–447.

(39) Baji, Z.; Lábadi, Z.; Horváth, Z. E.; Molnár, G.; Volk, J.; Bársony, I.; Barna, P. Nucleation and Growth Modes of ALD ZnO. *Cryst. Growth Des.* **2012**, *12*, 5615–5620.

(40) Islam, M. N.; Ghosh, T. B.; Chopra, K. L.; Acharya, H. N. XPS and X-Ray Diffraction Studies of Aluminum-Doped Zinc Oxide Transparent Conducting Films. *Thin Solid Films* **1996**, *280*, 20–25.

(41) Oh, I. K.; Tanskanen, J.; Jung, H.; Kim, K.; Lee, M. J.; Lee, Z.; Lee, S. K.; Ahn, J. H.; Lee, C. W.; Kim, K.; Kim, H.; Lee, H.-B.-R. Nucleation and Growth of the HfO_2 Dielectric Layer for Graphene-Based Devices. *Chem. Mater.* **2015**, *27*, 5868–5877.

(42) Lee, H. B. R.; Baeck, S. H.; Jaramillo, T. F.; Bent, S. F. Growth of Pt Nanowires by Atomic Layer Deposition on Highly Ordered Pyrolytic Graphite. *Nano Lett.* **2013**, *13*, 457–463.

(43) Kim, K.; Lee, H.-B.-R.; Johnson W. R.; Tanskanen, J. T.; Liu, N.; Kim, M.-G.; Pang, C.; Ahn, C.; Bent, S. F.; Bao, Z. Selective Metal Deposition at Graphene Line Defects by Atomic Layer Deposition. *Nat. Commun.* **2014**, *5*, 4781.

(44) Babonneau, D. FitGISAXS: Software Package for Modelling and Analysis of GISAXS Data Using IGOR Pro. *J. Appl. Crystallogr.* **2010**, *43*, 929–936.

(45) Zhang, J.; Wu, J.; Guo, H.; Chen, W.; Yuan, J.; Martinez, U.; Gupta, G.; Mohite, A.; Ajayan, P. M.; Lou, J. Unveiling Active Sites for the Hydrogen Evolution Reaction on Monolayer MoS_2. *Adv. Mater.* **2017**, *29*, 1–7.

(46) Kronberg, R.; Hakala, M.; Holmberg, N.; Laasonen, K. Hydrogen Adsorption on MoS_2-Surfaces: A DFT Study on Preferential Sites and the Effect of Sulfur and Hydrogen Coverage. *Phys. Chem. Chem. Phys.* **2017**, *19*, 16231–16241.

(47) McDonnell, S.; Brennan, B.; Azcatl, A.; Lu, N.; Dong, H.; Buie, C.; Kim, J.; Hinkle, C. L.; Kim, M. J.; Wallace, R. M. HfO_2 on MoS_2 by Atomic Layer Deposition: Adsorption Mechanisms and Thickness Scalability. *ACS Nano* **2013**, *7*, 10354–10361.

(48) Zhang, H.; Chiappe, D.; Meersschaut, J.; Conard, T.; Franquet, A.; Nuytten, T.; Mannarino, M.; Radu, I.; Vandervorst, W.; Delabie, A. Nucleation and Growth Mechanisms of Al_2O_3 Atomic Layer Deposition on Synthetic Polycrystalline MoS_2. *J. Chem. Phys.* **2017**, *146*, 052810.

(49) Park, T.; Kim, H.; Leem, M.; Ahn, W.; Choi, S.; Kim, J.; Uh, J.; Kwon, K.; Jeong, S. J.; Park, S.; Kim, Y.; Kim, H. Atomic Layer Deposition of Al_2O_3 on MoS_2, WS_2, WSe_2, and h-BN: Surface Coverage and Adsorption Energy. *RSC Adv.* **2017**, *7*, 884–889.

(50) Pung, S. Y.; Choy, K. L.; Hou, X.; Shan, C. Preferential Growth of ZnO Thin Films by the Atomic Layer Deposition Technique. *Nanotechnology* **2008**, *19*, 435609.

(51) Wang, H.; Yu, L.; Lee, Y. H.; Shi, Y.; Hsu, A.; Chin, M. L.; Li, L. J.; Dubey, M.; Kong, J.; Palacios, T. Integrated Circuits Based on Bilayer MoS_2 Transistors. *Nano Lett.* **2012**, *12*, 4674–4680.

(52) Ma, D.; Shi, J.; Ji, Q.; Chen, K.; Yin, J.; Lin, Y.; Zhang, Y.; Liu, M.; Feng, Q.; Song, X.; Guo, X.; Zhang, J.; Zhang, Y.; Liu, Z. A Universal Etching-Free Transfer of MoS_2 Films for Applications in Photodetectors. *Nano Res.* **2015**, *8*, 3662–3672.

(53) Ilavsky, J. Nika: Software for Two-Dimensional Data Reduction. *J. Appl. Crystallogr.* **2012**, *45*, 324–328.

(54) Renaud, G.; Lazzari, R.; Leroy, F. Probing Surface and Interface Morphology with Grazing Incidence Small Angle X-Ray Scattering. *Surf. Sci. Rep.* **2009**, *64*, 255–380.

(55) Toney, M. F.; Geyer, S. M.; Brennan, S.; Johnson, R.; Bent, S.; Methaapanon, R.; Clemens, B. Structural Evolution of Platinum Thin Films Grown by Atomic Layer Deposition. *J. Appl. Phys.* **2014**, *116*, 064905.

(56) Giannozzi, P.; Baroni, S.; Bonini, N.; Calandra, M.; Car, R.; Cavazzoni, C.; Ceresoli, D.; Chiarotti, G. L.; Cococcioni, M.; Dabo, I.; Corso, A. D.; Gironcoli, D. S.; Fabris, S.; Fratesi, G.; Gebauer, R.; Gerstmann, U.; Gougoussis, C.; Kokalj, A.; Lazzeri, M.; Martin-Samos, L.; *et al.* QUANTUM ESPRESSO: A Modular and Open-Source Software Project for Quantum Simulations of Materials. *J. Phys.: Condens. Matter* **2009**, *21*, 395502

(57) Perdew, J. P.; Burke, K.; Ernzerhof, M. Generalized Gradient Approximation Made Simple. *Phys. Rev. Lett.* **1996**, *77*, 3865–3868.

(58) Grimme, S. Semiempirical GGA-Type Density Functional Constructed with a Long-Range Dispersion Correction. *J. Comput. Chem.* **2009**, *27*, 1787–1799.

(59) Blöchl, P. E. Projector Augmented-Wave Method. *Phys. Rev. B* **1994**, *50*, 17953–17979.

(60) Lauritsen, J. V.; Kibsgaard, J.; Helveg, S.; Topsøe, H.; Clausen, B. S.; Lægsgaard, E.; Besenbacher, F. Size-Dependent Structure of MoS_2 Nanocrystals. *Nat. Nanotechnol.* **2007**, *2*, 53–58.

(61) Henkelman, G.; Uberuaga, B. P.; Jónsson, H. A Climbing Image Nudged Elastic Band Method for Finding Saddle Points and Minimum Energy Paths. *J. Chem. Phys.* **2000**, *113*, 9901–9904.

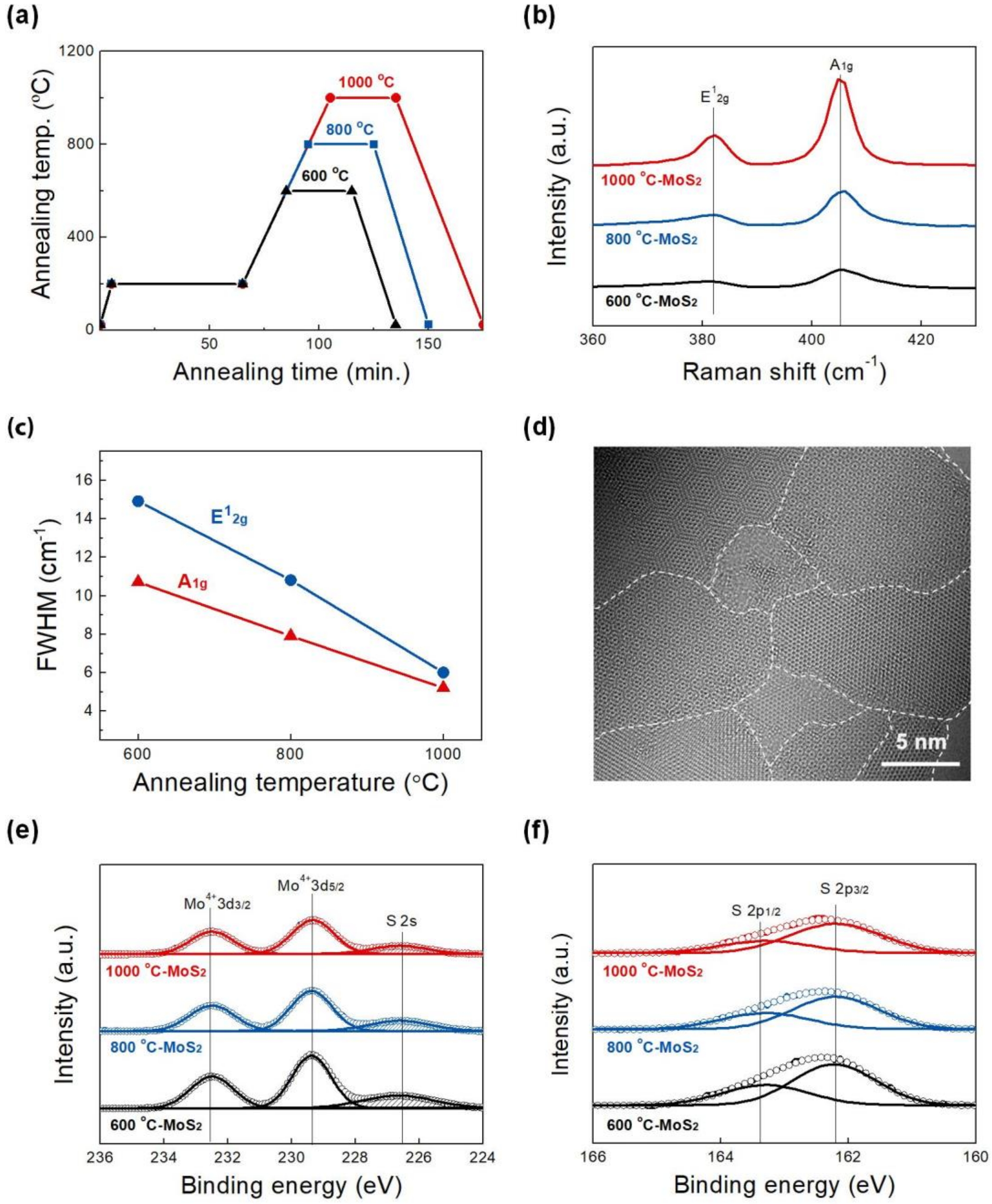

Figure 1. (a) A two-step synthesis process of MoS_2 by H_2S sulfurization from ALD MoO_3 at three different annealing temperatures, 600, 800, and 1000 °C. (b) Raman spectra for 600 °C-, 800 °C-, and 1000 °C-MoS_2. (c) FWHM values of the Raman peaks for MoS_2 annealed at different temperatures from Figure 1(b). (d) HR-STEM image of 800 °C-MoS_2 surface. Chemical composition analysis measured by XPS of 600 °C-, 800 °C-, and 1000 °C-MoS_2 for (e) Mo 3d and (f) S 2p core level spectra, respectively.

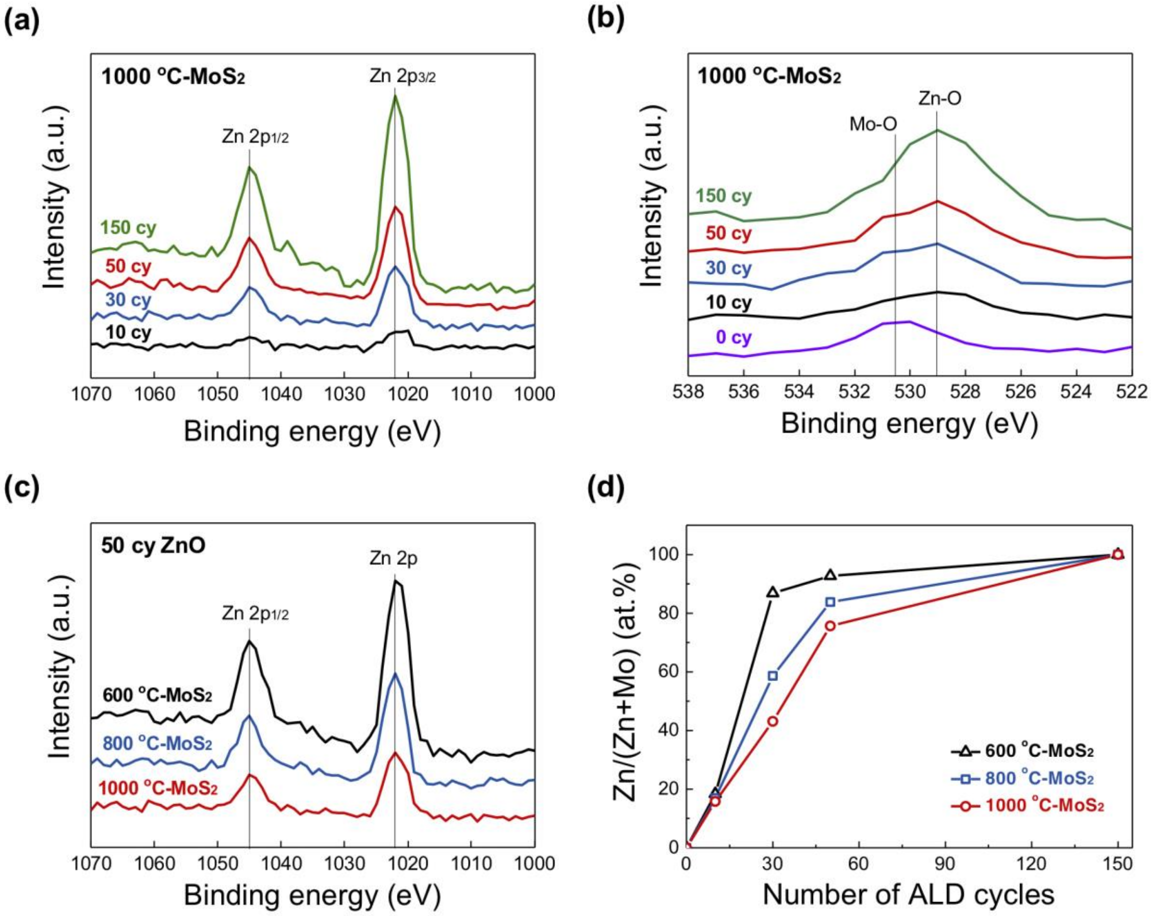

Figure 2. XPS results of 1000 °C-MoS$_2$ decorated with 10, 30, 50, and 150 cycles ALD ZnO for (a) Zn 2p and (b) O 1s core level spectra. XPS results of 600 °C-, 800 °C-, and 1000 °C-MoS$_2$ with 50 cycles ALD ZnO for (c) Zn 2p core level spectra. (d) Relative atomic percentage of Zn/(Zn+Mo) for ALD ZnO on 600 °C-, 800 °C-, and 1000 °C-MoS$_2$.

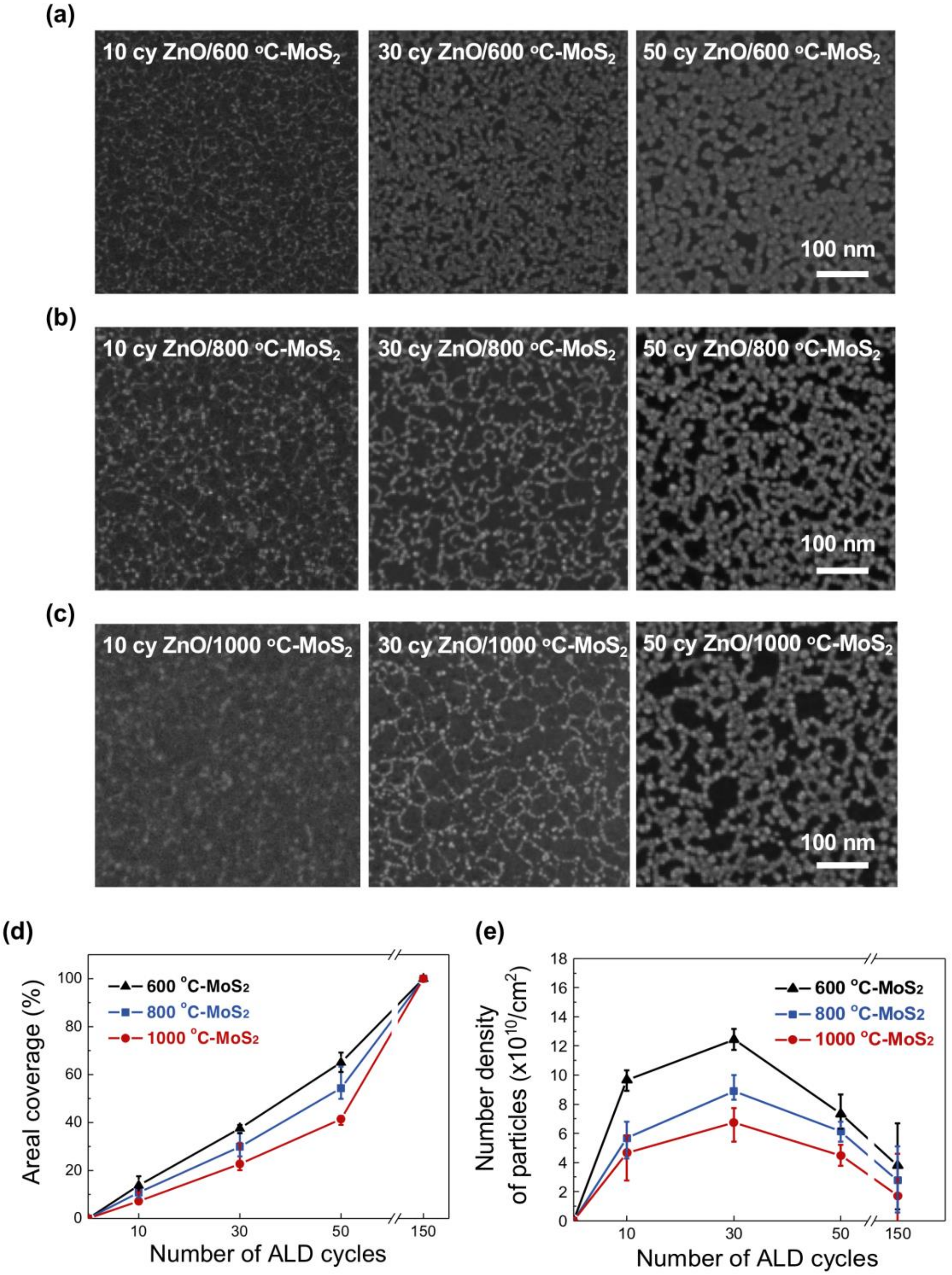

Figure 3. SEM images of ALD ZnO on three MoS_2 samples with increasing ZnO ALD cycles (for 10, 30, and 50 cycles from left to right) on (a) 600 °C-, (b) 800 °C-, and (c) 1000 °C-MoS_2. (d) Extracted areal coverages and (e) number density of ZnO particles on the MoS_2 surfaces. Scale bars for all images in (a) through (c) are the same.

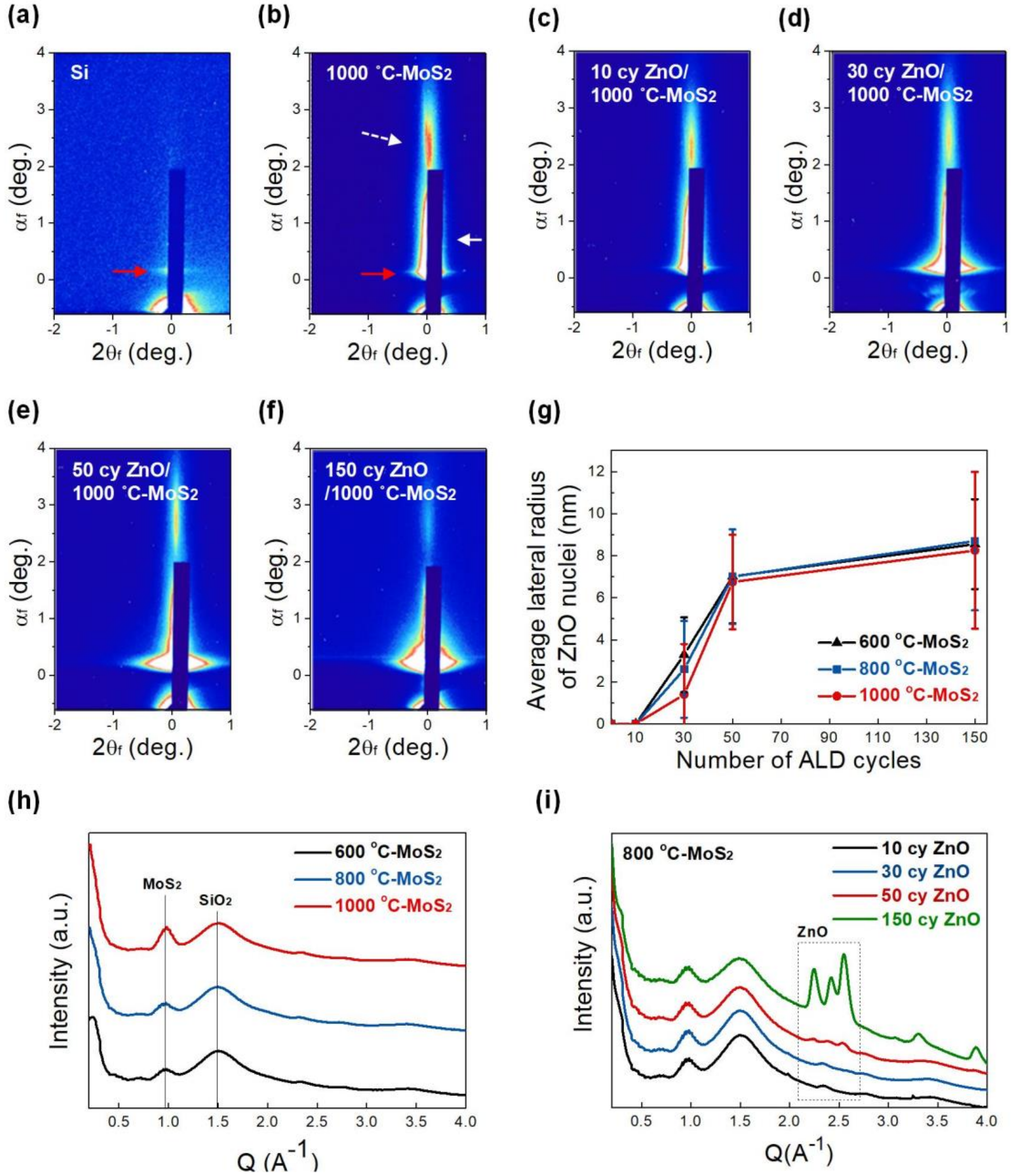

Figure 4. GISAXS patterns of (a) Si substrate and (b) 1000 °C-MoS_2 nanosheets on Si. The horizontal Yoneda peaks ($\alpha_f = \alpha_c$), reflected beam ($\alpha_f = \alpha_i = 0.6°$), and film fringes are indicated by red arrows, white solid arrows, and white dashed arrows, respectively. GISAXS patterns after ALD ZnO on 1000 °C-MoS_2 for (c) 10, (d) 30, (e) 50, and (f) 150 cycles. (g) Average lateral radius of ZnO nuclei on 600 °C-, 800 °C-, and 1000 °C-MoS_2 with increasing ZnO ALD cycle numbers, measured by GISAXS. GIWAXS patterns of (h) 600 °C-, 800 °C-, and 1000 °C-MoS_2 and (i) ZnO on 800 °C-MoS_2 with increasing ALD cycle numbers.

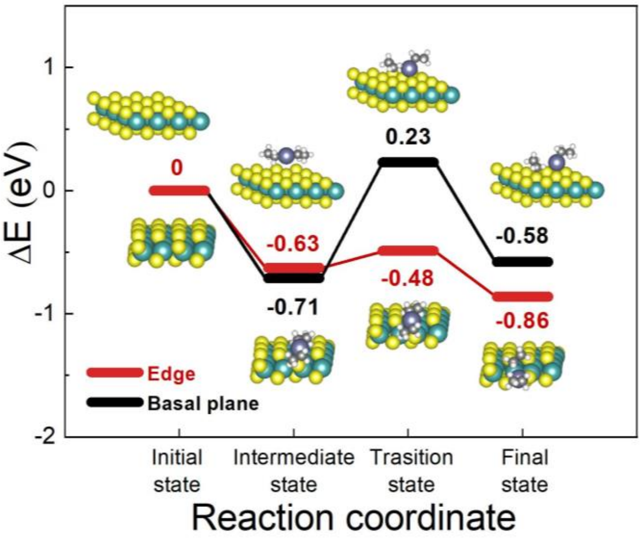

Figure 5. Quantum chemical calculation results of DEZ reaction on edge sites and basal planes of MoS_2 by DFT. Yellow and green atoms indicate S and Mo, respectively.

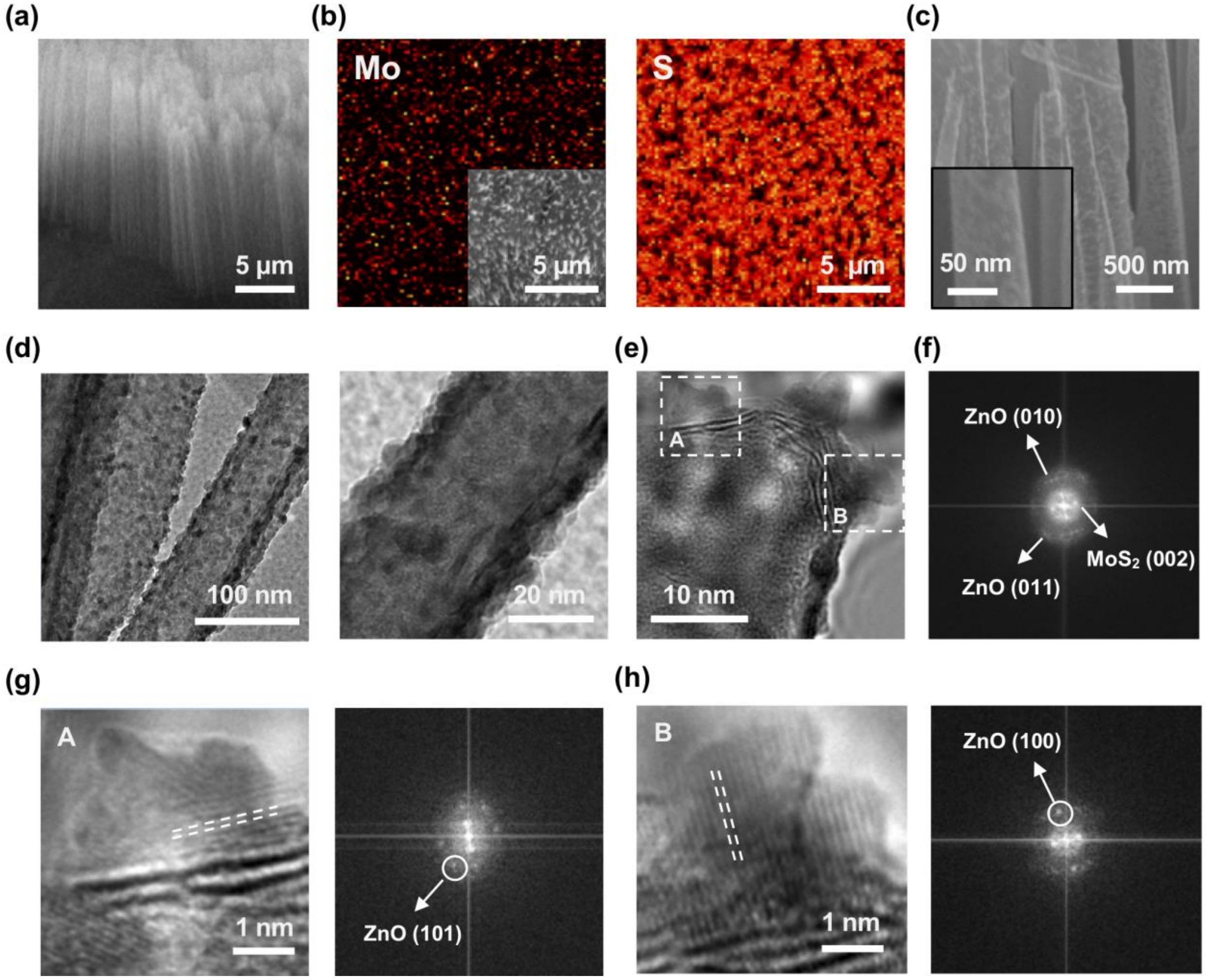

Figure 6. (a) SEM image of 800 °C-MoS$_2$ NWs. (b) Elemental signals of Mo and S detected by EDS for top-view image of 800 °C-MoS$_2$ NWs shown in the inset of Figure 6(b). (c) Magnified SEM image of 800 °C-MoS$_2$ NWs after 30 cycles of ZnO ALD with a higher magnification image shown in the inset. HR-STEM images of 30 ALD cycles ZnO on 800 °C-MoS$_2$ NWs along (d) horizontal and (e) vertical directions of the NWs. (f) FFT of the HR-STEM image of Figure 6(e). (g) and (h) Magnified images obtained in the A and B boxes in Figure 6(e) and their FFT images, respectively.

Table of Contents